(Preprint) AAS 25-786

PLANAR SPACECRAFT CONTROL THROUGH ONE DEGREE OF FREEDOM TIME-VARYING THRUSTER CONFIGURATIONS

William R. Schwend* **and Hanspeter Schaub†**

This paper investigates the use of thrusters mounted on one-degree of freedom robotic manipulators for planar control of the position and orientation of a spacecraft. The proposed solution addresses the fuel consumption and mass concerns of fixed thruster configurations. An analysis of the dynamics of the system and a cascaded control design is performed with the coupling of spacecraft and manipulator dynamics being addressed through the incorporation of a prescribed torque to negate the hub accelerations that result from arm motion. The stability of the control is analyzed using both linear and Lyapunov methods. Numerical simulations are used to validate the control design for both regulation and tracking problems and evaluate the viability of various momentum exchange devices in mitigating the effects of reaction torques.

INTRODUCTION

As more ambitious mission concepts begin to be realized that make it infeasible for the launch of a fully operational system, new cost-effective ways to update capabilities on-orbit need to be developed. In-space Servicing, Assembly, and Manufacturing (ISAM) can improve performance, provide repairs, and extend mission lifetime[1] over more traditional methods of never touching the system after launch making it a priority for commercial space missions[2] in addition to several nation's National Security interests.[3] These emerging mission concepts often rely on physical grappling of other on-orbit objects as shown in the Hubble Space Telescope upgrades as well as Northrop Grumman's new Mission Extension Vehicle (MEV).[4] One of the key considerations for the spacecraft performing these missions is their ability to carefully operate while within a few craft radii of separation distance with minimal human oversight. Traditional positional and attitude control methods for these missions rely on thruster clusters where the configuration is fixed relative to the maneuvering spacecraft.[5,6] While these fixed thruster configurations can take advantage of established algorithms for mapping forces and torques to finite thruster burns that are computationally inexpensive,[7] these body-fixed configurations demand a large number of thrusters to meet maneuverability requirements and result in increased Δv expenditure.[8]

Recently, more complex thruster configurations have been proposed to reduce the number of required thrusters. These proposed configurations take advantage of the robotic manipulators often already on-board the spacecraft by placing thrusters at the ends of the manipulators[9–17] as shown in Figure 1. These more complex time-varying configurations enable thrusters to be positioned in a manner that allows them to more directly produce the control wrench required by the mission, maintaining the spacecraft's maneuverability, while reducing the number of thrusters and Δv required to perform operations.[12–17]

The close proximity operations required for ISAM require the servicing spacecraft to fly a target object relative path so that they can approach and hold a fixed position and orientation relative to the object onto which the servicer will dock. Such non-Keplerian motion is challenging to control even when using fixed thruster configurations as it requires coupled relative orbit and attitude control.[18] This task is made more

*PhD Student, Ann and H.J. Smead Department of Aerospace Engineering Sciences, University of Colorado Boulder, 3775 Discovery Dr, Boulder, CO 80303.

†Distinguished Professor and Department Chair, Ann and H.J. Smead Department of Aerospace Engineering Sciences, University of Colorado Boulder, 3775 Discovery Dr, Boulder, CO 80303.

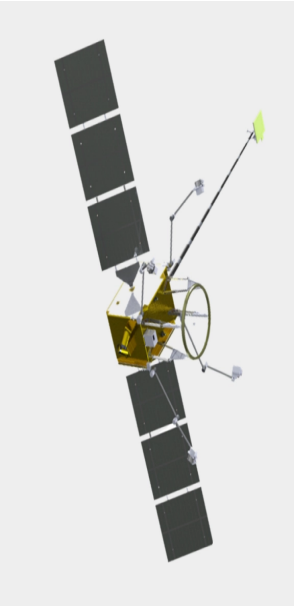

(a) Astroscale Lexi[9]

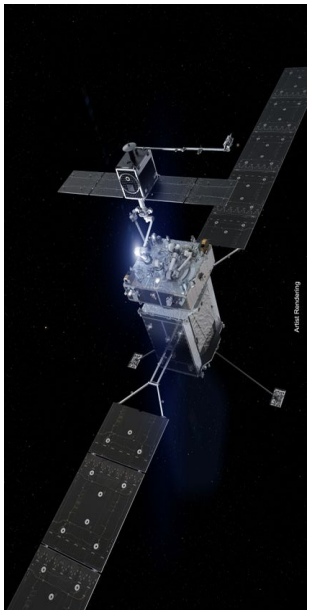

(b) Northrup Grumman MEV and MEP[10]

Figure 1: Model renders of proposed spacecraft with thrusters on robotic arms

complex once time-varying thruster configurations, such as thrusters on robotic manipulators, begin to be used. Due to the coupling between the motion of the robotic manipulator and the spacecraft hub, novel control systems must be designed to ensure the relative orientation between the servicer and the object to be grappled remains fixed. Significant work in this field has been performed studying the design of control systems for spacecraft with attached robotic manipulators.[19–22] These formulations still rely on traditional control methods, however, and do not utilize the robotic manipulators for control actuation.

Several studies have been conducted that take advantage of variable thruster configurations. Calaon et al.[23] studied the use of thrusters mounted on a dual gimbaled platform for spacecraft momentum management. However, the proposed control method relied on continuous thrust from the main electric thruster on the spacecraft making it well suited to long-duration missions but ill fitted to proximity operations. Wei et al.[16] and Caverly et al.[12–14] used thrusters mounted on robotic arms for joint station keeping and momentum management of GEO spacecraft. These methods, however, took advantage of the long duration between station keeping burns, often on the order of several hours, allowing for slow arm repositioning limiting the torque impact on the spacecraft hub. This allowed them to utilize reaction wheels to assist with hub attitude control. The necessity for faster arm repositioning when operating in close proximity leads to torques that well exceed the control capability of reaction wheels, however. Finally, Prakash and Giri[17] formulated a loop dynamics approach that did not rely on external momentum transfer devices to accomplish attitude control. This approach leaves the spacecraft hub free to experience acceleration during arm motion, something that is undesirable when operating in close proximity to another spacecraft and trying to keep precise sensor alignment and ensure proper separation.

This paper studies a planar coupled control design for a spacecraft with thrusters mounted on one-degree-of-freedom (1-DOF) robotic arms. Looking at one-dimensional rotational motion challenges is illustrative, but the long-term goal is developing a solution that can scale to three-dimensional rotations. The often large and rapid repositioning required of the arms for operation in close proximity to other spacecraft, coupled with the need to maintain a desired hub attitude, necessitates the inclusion of additional momentum management systems. To this end a prescribed torque is utilized to offset undesirable hub accelerations during arm motion, allowing the spacecraft to safely operate in close proximity to other spacecraft. What follows begins with the

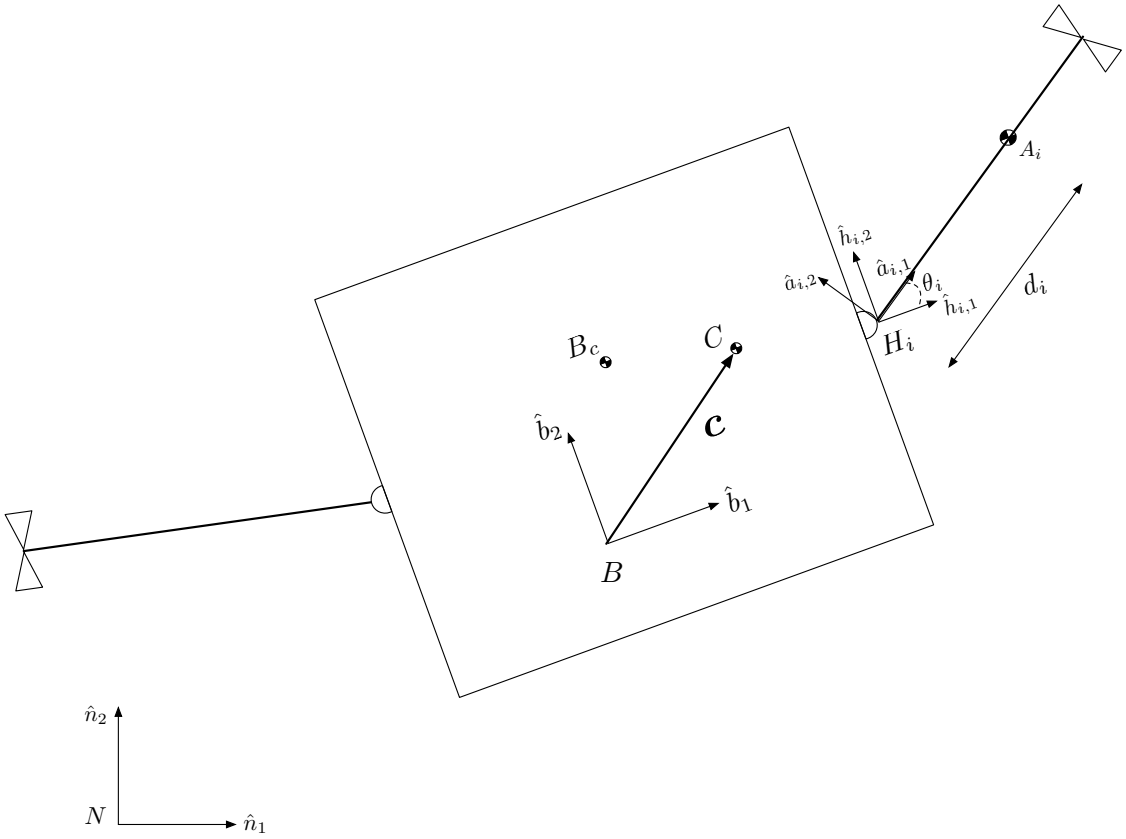

Figure 2: Variables and coordinate frames for the equation of motion derivation

formulation of the planar equations of motion (EOM), followed by a brief discussion of control allocation. Next, a cascaded control loop is designed that utilizes a prescribed torque to allow for large and rapid arm repositioning without affecting the spacecraft hub's motion. Finally, numerical simulations for both a regulation and tracking control problem are performed, with the results analyzed for both control accuracy as well as control effort.

PLANAR EQUATIONS OF MOTION

This section develops the planar EOMs using Newtonian and Eulerian mechanics. EOMs are required for the spacecraft translation, hub rotation and the arm motion. Figure 2 introduces the coordinate frames and variables used for this formulation.

The spacecraft in Figure 2 has a rigid spacecraft hub with two 1-DOF arms mounted to it, each with 2 thrusters. The joints are modeled as motors which can produce a motor torque u_{H_i}. While only two arms are shown the formulation allows for N_a number of arms. There are four coordinate frames used throughout the remainder of this paper. The inertial frame $\mathcal{N} : \{\hat{n}_1, \hat{n}_2, \hat{n}_3\}$, with origin N is the basis from which the dynamics are developed. The body fixed frame $\mathcal{B} : \{\hat{b}_1, \hat{b}_2, \hat{n}_3\}$ has origin B and can be located anywhere on the spacecraft hub, which has mass m_{hub}. The ith arm frame, with mass m_{a_i}, is mounted at the ith hinge joint H_i with hinge joint frame $\mathcal{H}_i : \{\hat{h}_{i,1}, \hat{h}_{i,2}, \hat{n}_3\}$. $\mathcal{H}_i$ is fixed with respect to the $\mathcal{B}$ and is equivalent to the arm frame $\mathcal{A}_i : \{\hat{a}_{i,1}, \hat{a}_{i,2}, \hat{n}_3\}$ when the angle between the two frames $\theta_i = 0$. All coordinate frames share the third axis $\hat{n}_3$ which points out of the page in Figure 2.

The location of the total spacecraft center of mass is C, and B_c is the body-fixed spacecraft hub center of mass. The vector $\boldsymbol{c}$ that points from B to C. The variable A_i is the combined center of mass for the i^{th} arm

plus the attached thrusters and is located a distance d_i away from the hinge H_i.

Spacecraft Translational Equations of Motion

Using Newton's second law for the center of mass of the spacecraft the translational EOMs are:

$$\boldsymbol{F}_{\text{ext}} = m_{\text{sc}}\ddot{\boldsymbol{r}}_{C/N} \tag{1}$$

where $\boldsymbol{r}_{C/N}$ is the vector pointing from point N to point C, $\boldsymbol{F}_{\text{ext}}$ is the sum of all external forces acting on the spacecraft, and m_{sc} is the total spacecraft mass:

$$m_{\text{sc}} = m_{\text{hub}} + \sum_{i=1}^{N_a} m_{\text{a}_i} \tag{2}$$

The frame-independent vector equation for the translational motion of the spacecraft center of mass is fully decoupled from the hub rotational motion as well as the motion of the arms.

Hub Rotational Equations of Motion

Next, the rigid body rotational motion of the hub are developed. The derivation begins with Euler's equation for a body-fixed coordinate system not coincident with the center of mass of the body[24] :

$$\dot{\boldsymbol{H}}_{\text{sc},B} = \boldsymbol{L}_B + m_{\text{sc}}\ddot{\boldsymbol{r}}_{B/N} \times \boldsymbol{c} \tag{3}$$

where $\boldsymbol{H}_{\text{sc},B}$ is the angular momentum of the spaacecraft about point B and:

$$\ddot{\boldsymbol{r}}_{B/N} = \ddot{\boldsymbol{r}}_{C/N} - \ddot{\boldsymbol{c}} \tag{4}$$

the center of mass vector $\boldsymbol{c}$ is:

$$\boldsymbol{c} = \frac{m_{\text{hub}}\boldsymbol{r}_{B_c/B} + \sum_{i=1}^{N_a} m_{\text{a}_i}\boldsymbol{r}_{A_i/B}}{m_{\text{sc}}} \tag{5}$$

and $\boldsymbol{L}_B$ is the total external torque about point B. Substituting Eq. (4) into Eq. (3) results in:

$$\dot{\boldsymbol{H}}_{\text{sc},B} = \boldsymbol{L}_B + m_{\text{sc}}(\ddot{\boldsymbol{r}}_{C/N} - \ddot{\boldsymbol{c}}) \times \boldsymbol{c} \tag{6}$$

Following the derivation by Allard et al.[25] and using the vector:

$$\boldsymbol{r}_{A_i/H} = d_i\hat{\boldsymbol{a}}_{i,1} \tag{7}$$

The inertial second time derivative of $\boldsymbol{c}$ is expressed as:

$$\ddot{\boldsymbol{c}} = \boldsymbol{c}'' + 2\boldsymbol{\omega}_{B/N} \times \boldsymbol{c}' + \dot{\boldsymbol{\omega}}_{B/N} \times \boldsymbol{c} + \boldsymbol{\omega}_{B/N} \times (\boldsymbol{\omega}_{B/N} \times \boldsymbol{c}) \tag{8}$$

where $\boldsymbol{\omega}_{B/N}$ is the angular velocity of the $\mathcal{B}$ frame relative to the $\mathcal{N}$ and the body relative first and second time derivatives of $\boldsymbol{c}$ are:

$$\boldsymbol{c}' = \frac{\sum_{i=1}^{N_a} m_{\text{a}_i} d_i\dot{\theta}_i\hat{\boldsymbol{a}}_{i,2}}{m_{\text{sc}}} \qquad \boldsymbol{c}'' = \frac{\sum_{i=1}^{N_a} m_{\text{a}_i} d_i(\ddot{\theta}_i\hat{\boldsymbol{a}}_{i,2} - \dot{\theta}_i^2\hat{\boldsymbol{a}}_{i,1})}{m_{\text{sc}}} \tag{9}$$

The angular momentum vector of the spacecraft about point B is :

$$\begin{aligned}\boldsymbol{H}_{\text{sc},B} =& [I_{\text{hub},B_c}]\boldsymbol{\omega}_{B/N} + m_{\text{hub}}\boldsymbol{r}_{B_c/B} \times \dot{\boldsymbol{r}}_{B_c/B} \\ &+ \sum_{i=1}^{N_a}([I_{\text{a}_i,A_i}]\boldsymbol{\omega}_{B/N} + \dot{\theta}_i I_{a_{i,3}}\hat{n}_3 + m_{\text{a}_i}\boldsymbol{r}_{A_i/B} \times \dot{\boldsymbol{r}}_{A_i/B})\end{aligned} \tag{10}$$

where $[I_{\text{hub},B_c}]$ is the inertia of the spacecraft hub about its center of mass.

The arm frame $\mathcal{A}_i$ is assumed to be principal such that the arm inertia matrix about its center of mass when defined in the $\mathcal{A}_i$ frame is:

$$^{\mathcal{A}_\mathrm{i}}[I_{\mathrm{a}_i,A_i}] = \begin{matrix}\mathcal{A}_\mathrm{i}\\ \\ \\ \end{matrix}\begin{bmatrix} I_{a_{i,1}} & 0 & 0 \\ 0 & I_{a_{i,2}} & 0 \\ 0 & 0 & I_{a_{i,3}} \end{bmatrix} \tag{11}$$

Similarly the body frame $\mathcal{B}$ is assumed to be principal in the $\hat{n}_3$ direction. Substituting this definition and the value of $\boldsymbol{\omega}_{B/N} = [0, 0, \dot{\phi}]^T$ into Eq. (10) leads to:

$$\boldsymbol{H}_{\mathrm{sc},B} = I_{\mathrm{hub},3}\dot{\phi}\hat{n}_3 + m_{\mathrm{hub}}\boldsymbol{r}_{B_c/B} \times \dot{\boldsymbol{r}}_{B_c/B} + \sum_{i=1}^{N_a}(I_{a_{i,3}}(\dot{\phi} + \dot{\theta}_i)\hat{n}_3 + m_{\mathrm{a_i}}\boldsymbol{r}_{A_i/B} \times \dot{\boldsymbol{r}}_{A_i/B}) \tag{12}$$

Taking the time derivative of Eq. (12)

$$\dot{\boldsymbol{H}}_{\mathrm{sc},B} = I_{\mathrm{hub},3}\ddot{\phi}\hat{n}_3 + m_{\mathrm{hub}}\boldsymbol{r}_{B_c/B} \times \ddot{\boldsymbol{r}}_{B_c/B} + \sum_{i=1}^{N_a}(I_{a_{i,3}}(\ddot{\phi} + \ddot{\theta}_i)\hat{n}_3 + m_{\mathrm{a_i}}\boldsymbol{r}_{A_i/B} \times \ddot{\boldsymbol{r}}_{A_i/B}) \tag{13}$$

The terms $\ddot{\boldsymbol{r}}_{B_c/B}$ and $\ddot{\boldsymbol{r}}_{A_i/B}$ are found using the transport theorem[24] taking advantage of $\boldsymbol{r}_{B_c/B}$ being fixed in the body frame:

$$\ddot{\boldsymbol{r}}_{B_c/B} = \ddot{\phi}\hat{n}_3 \times \boldsymbol{r}_{B_c/B} + \dot{\phi}\hat{n}_3 \times (\dot{\phi}\hat{n}_3 \times \boldsymbol{r}_{B_c/B}) \tag{14}$$

$$\ddot{\boldsymbol{r}}_{A_i/B} = \boldsymbol{r}''_{A_i/B} + 2\dot{\phi}\hat{n}_3 \times \boldsymbol{r}'_{A_i/B} + \ddot{\phi}\hat{n}_3 \times \boldsymbol{r}_{A_i/B} + \dot{\phi}\hat{n}_3 \times (\dot{\phi}\hat{n}_3 \times \boldsymbol{r}_{A_i/B}) \tag{15}$$

Substituting Eqs. (14) and (15) into Eq. (13) and simplifying by taking advantage of the planar nature of the problem yields:

$$\begin{aligned}\dot{\boldsymbol{H}}_{\mathrm{sc},B} =& I_{\mathrm{hub},3}\ddot{\phi}\hat{n}_3 + m_{\mathrm{hub}}\boldsymbol{r}_{B_c/B} \times \ddot{\phi}\hat{n}_3 \times \boldsymbol{r}_{B_c/B} + \sum_{i=1}^{N_a}(I_{a_{i,3}}(\ddot{\phi} + \ddot{\theta}_i)\hat{n}_3 \\ &+ m_{\mathrm{a_i}}\boldsymbol{r}_{A_i/B} \times \boldsymbol{r}''_{A_i/B} + \boldsymbol{r}_{A_i/B} \times 2\dot{\phi}\hat{n}_3 \times \boldsymbol{r}'_{A_i/B} + m_{\mathrm{a_i}}\boldsymbol{r}_{A_i/B} \times \ddot{\phi}\hat{n}_3 \times \boldsymbol{r}_{A_i/B})\end{aligned} \tag{16}$$

where

$$\boldsymbol{r}'_{A_i/B} = d_i\dot{\theta}_i\hat{a}_{i,2} \tag{17}$$

$$\boldsymbol{r}''_{A_i/B} = d_i(\ddot{\theta}_i\hat{a}_{i,2} - \dot{\theta}_i^2\hat{a}_{i,1}) \tag{18}$$

Using the parallel axis theorem for the inertia matrices[24] a new frame independent inertia matrix for the spacecraft about point B can be developed as:

$$[I_{\mathrm{hub},B}] = [I_{\mathrm{hub},B_c}] + m_{\mathrm{hub}}[\tilde{\boldsymbol{r}}_{B_c/B}][\tilde{\boldsymbol{r}}_{B_c/B}]^T \tag{19}$$

$$[I_{\mathrm{a_i},B}] = [I_{\mathrm{a_i},A_i}] + m_{\mathrm{a_i}}[\tilde{\boldsymbol{r}}_{A_i/B}][\tilde{\boldsymbol{r}}_{A_i/B}]^T \tag{20}$$

$$[I_{\mathrm{sc},B}] = [I_{\mathrm{hub},B}] + \sum_{i=1}^{N_a}[I_{\mathrm{a_i},B}] \tag{21}$$

Here we make use of the skew-symmetric matrix definition : $\boldsymbol{u} \times \boldsymbol{v}$ is the crossproduct between $\boldsymbol{u}$ and $\boldsymbol{v}$ and can be expressed as $[\tilde{\boldsymbol{u}}]\boldsymbol{v}$ where $[\tilde{\boldsymbol{u}}]$ is the skew-symmetric matrix built from $\boldsymbol{u}$.

Due to the planar nature of the problem $[I_{\mathrm{sc},B}]$ is principal about the $\hat{n}_3$ axis. The element in the $(3,3)$ position $I_{\mathrm{sc},3}$ is extracted and reduces Eq. (16) to:

$$\begin{aligned}\dot{\boldsymbol{H}}_{\mathrm{sc},B} = I_{\mathrm{sc},3}\,\ddot{\phi}\,\hat{n}_3 + \sum_{i=1}^{N_a}\Big(&\big(I_{a_{i,3}}\hat{n}_3 + m_{\mathrm{a_i}}\,(\boldsymbol{r}_{A_i/B} \times \hat{a}_{i,2})\big)\,\ddot{\theta}_i \\ &- m_{\mathrm{a_i}}\,d_i\,\dot{\theta}_i^2\,(\boldsymbol{r}_{A_i/B} \times \hat{a}_{i,1}) + 2\,\dot{\phi}\,m_{\mathrm{a_i}}\,d_i\,\dot{\theta}_i\,\big(\boldsymbol{r}_{A_i/B} \times (\hat{n}_3 \times \hat{a}_{i,2})\big)\Big)\end{aligned} \tag{22}$$

Equating Eqs. (6) and (22), moving all second order derivative to the left hand side, and taking the dot product with $\hat{n}_3$ since all rotation is about that axis:

$$\begin{aligned}&\hat{n}_3 \cdot (m_{\text{sc}}\boldsymbol{c} \times (\ddot{\boldsymbol{r}}_{C/N} - \ddot{\boldsymbol{c}}) + I_{\text{sc},3}\ddot{\phi}\hat{n}_3 + \sum_{i=1}^{N_a}(I_{a_{i,3}}\hat{n}_3 + m_{\text{a}_i}\boldsymbol{r}_{A_i/B} \times \hat{a}_{i,2})\ddot{\theta}_i)\\ &= \hat{n}_3 \cdot (\boldsymbol{L}_B - \sum_{i=1}^{N_a} 2\dot{\phi}m_{\text{a}_i}d_i\dot{\theta}_i\boldsymbol{r}_{A_i/B} \times (\hat{n}_3 \times \hat{a}_{i,2}) - m_{\text{a}_i}d_i\dot{\theta}_i^2\boldsymbol{r}_{A_i/B} \times \hat{a}_{i,1})\end{aligned} \tag{23}$$

This frame-independent vector equation for the planar rotational motion for the spacecraft hub with N_a attached arms demonstrates the coupling that arises due to the multi-body interaction of the rigid bub and the moving arms.

Arm Equations of Motion

The final set of EOMs needed to solve the full system of differential equations is for the 1-DOF arms. In this derivation the ith arm frame A_i is assumed to be a principal frame leading to the diagonal inertia matrix provided in Eq. (11). Let the total torque acting about hinge point H_i be:

$$\boldsymbol{L}_{H_i} = L_{i,1}\hat{a}_{i,1} + L_{i,2}\hat{a}_{i,2} + L_{i,3}\hat{n}_3 \tag{24}$$

The hinge torque component acting about the inertially and body fixed hinge axis $\hat{n}_3$ is:

$$L_{i,3} = u_{H_i} + L_{f_i} + \hat{n}_3 \cdot \boldsymbol{\tau}_{\text{ext}} \tag{25}$$

where u_{H_i} is the torque produced by the motor at the hinge, L_{f_i} is the torque about the hinge produced by the firing of the thrusters, and $\hat{n}_3 \cdot \boldsymbol{\tau}_{\text{ext}}$ is the total external torque acting on the arm projected onto the $\hat{n}_3$ direction. The structure of the hinge would produce the other two torques $L_{i,1}$ and $L_{i,2}$.

The inertial angular velocity vector of the arm is:

$$\boldsymbol{\omega}_{A_i/N} = \boldsymbol{\omega}_{A_i/H_i} + \boldsymbol{\omega}_{H_i/B} + \boldsymbol{\omega}_{B/N} \tag{26}$$

where $\boldsymbol{\omega}_{H_i/B} = \boldsymbol{0}$ since the hinge frame $\mathcal{H}_i$ is fixed with respect to the body leading to:

$$\boldsymbol{\omega}_{A_i/N} = (\dot{\phi} + \dot{\theta}_i)\hat{n}_3 \tag{27}$$

Substituting the angular velocity into the rotational equations of motion of a rigid body with torques about the center of mass[24] and noting that the first two equations are zero due to the planar nature of the problem the general equation of motion for the arm is:

$$I_{a_{i,3}}(\ddot{\phi} + \ddot{\theta}_i) = L_{a_{i,3}} \tag{28}$$

where

$$\boldsymbol{L}_{A_i} = L_{a_{i,1}}\hat{a}_{i,1} + L_{a_{i,2}}\hat{a}_{i,2} + L_{a_{i,3}}\hat{n}_3 \tag{29}$$

The torque about the arm center of mass can related to the torque about the hinge through:

$$\boldsymbol{L}_{A_i} = \boldsymbol{L}_{H_i} - \boldsymbol{r}_{A_i/H_i} \times m_{\text{a}_i}\ddot{\boldsymbol{r}}_{A_i/N} \tag{30}$$

Finding the projection of Eq. (30) onto $\hat{n}_3$ and using Eq. (7) leads to the scalar equation:

$$L_{a_{i,3}} = u_{H_i} + L_{f_i} + \hat{n}_3 \cdot \boldsymbol{\tau}_{\text{ext}} - m_{\text{a}_i}d_i\hat{n}_3 \cdot (\hat{a}_{i,1} \times \ddot{\boldsymbol{r}}_{A_i/N}) \tag{31}$$

Making use of $\boldsymbol{r}_{A_i/N} = \boldsymbol{r}_{H_i/N} + \boldsymbol{r}_{A_i/H_i}$:

$$\ddot{\boldsymbol{r}}_{A_i/N} = \ddot{\boldsymbol{r}}_{H_i/N} + (\ddot{\phi} + \ddot{\theta}_i)\hat{n}_3 \times d_i\hat{a}_{i,1} + (\dot{\phi} + \dot{\theta}_i)\hat{n}_3 \times \Big((\dot{\phi} + \dot{\theta}_i)\hat{n}_3 \times d_i\hat{a}_{i,1}\Big) \tag{32}$$

Substituting Eq. (32) into Eq. (31) and making use of the identity $\boldsymbol{u} \cdot (\boldsymbol{v} \times \boldsymbol{w}) = (\boldsymbol{u} \times \boldsymbol{v}) \cdot \boldsymbol{w}$:

$$L_{a_{i,3}} = u_{H_i} + L_{f_i} + \hat{n}_3 \cdot \boldsymbol{\tau}_{\text{ext}} - m_{\text{a}_i} d_i \hat{a}_{i,2} \cdot \ddot{\boldsymbol{r}}_{H_i/N} - m_{\text{a}_i} d_i^2 (\ddot{\phi} + \ddot{\theta}_i) \tag{33}$$

Substituting this torque back into Eq. (28) produces:

$$(I_{a_{i,3}} + m_{\text{a}_i} d_i^2)(\ddot{\phi} + \ddot{\theta}_i) + m_{\text{a}_i} d_i \hat{a}_{i,2} \cdot \ddot{\boldsymbol{r}}_{H_i/N} - u_{H_i} - L_{f_i} - \hat{n}_3 \cdot \boldsymbol{\tau}_{\text{ext}} = 0 \tag{34}$$

Finally, using $\boldsymbol{r}_{H_i/N} = (\boldsymbol{r}_{C/N} - \boldsymbol{c}) + \boldsymbol{r}_{H_i/B}$ and taking advantage of the hinge being fixed in the body frame leads to:

$$\begin{aligned} m_{\text{a}_i} d_i \hat{a}_{i,2} \cdot (\ddot{\boldsymbol{r}}_{C/N} - \ddot{\boldsymbol{c}}) + (I_{a_{i,3}} + m_{\text{a}_i} d_i^2)(\ddot{\phi} + \ddot{\theta}_i) + m_{\text{a}_i} d_i \dot{\phi} \hat{a}_{i,1} \cdot \boldsymbol{r}_{H_i/B} \\ = u_{H_i} + L_{f_i} + \hat{n}_3 \cdot \boldsymbol{\tau}_{\text{ext}} + m_{\text{a}_i} d_i \dot{\phi}^2 \hat{a}_{i,2} \cdot \boldsymbol{r}_{H_i/B} \end{aligned} \tag{35}$$

This scalar equation provides the N_a arm EOMs needed to fully describe the motion of the spacecraft.

JOINT AND THRUSTER ALLOCATION

This section focuses on the methods to select the joint angles and thrust magnitude for each thruster on the spacecraft.

Coupled Joint and Thruster Allocation

Following the approach developed by Caverly et al.[14] the selection of joint angles and thruster firings can be done by solving an optimization problem:

$$\min_{\boldsymbol{\theta}, \boldsymbol{f}} (\boldsymbol{u}_{\text{des}} - \boldsymbol{u}_{\text{control}}(\boldsymbol{\theta}, \boldsymbol{f}))^T \boldsymbol{W}_u (\boldsymbol{u}_{\text{des}} - \boldsymbol{u}_{\text{control}}(\boldsymbol{\theta}, \boldsymbol{f})) + \boldsymbol{W}_f^T \boldsymbol{f} \tag{36}$$

subject to

$$\begin{aligned} \boldsymbol{\theta}_{\min} \leq \boldsymbol{\theta} \leq \boldsymbol{\theta}_{\min} \\ 0 \leq \boldsymbol{f} \leq \boldsymbol{f}_{\max} \end{aligned} \tag{37}$$

where $\boldsymbol{u}_{\text{des}} \in \mathbb{R}^{6\times 1}$ is the desired control wrench, $\boldsymbol{u}_{\text{control}}(\boldsymbol{\theta}, \boldsymbol{f}) \in \mathbb{R}^{6\times 1}$ is the control wrench produced by the N_j joint angles, $\boldsymbol{\theta} \in \mathbb{R}^{N_j \times 1}$, and M thruster forces, $\boldsymbol{f} \in \mathbb{R}^{M\times 1}$, and $\boldsymbol{W}_u \in \mathbb{R}^{6\times 6}$,$\boldsymbol{W}_f \in \mathbb{R}^{M\times 1}$ are the weighting matrices corresponding to the control and thruster actuation respectively.

This optimization problem can then be solved using a standard off the shelf solver with methods such as multi-start sequential quadratic programing (SQP) to avoid local minima.

Decoupled Joint and Thruster Allocation

When using 1-DOF arms it is possible to choose the joint angles and thrust magnitudes separately and still arrive at an optimal solution, so long as the arm and thruster configuration is such that any force vector can be directly accessed while producing zero torque. In these instances the desired control wrench is:

$$\boldsymbol{u}_{\text{des}} = \begin{bmatrix} \boldsymbol{F}_{\text{des}} \\ \boldsymbol{L}_{\text{des}} \end{bmatrix} \tag{38}$$

in inertial space $\boldsymbol{F}$ and $\boldsymbol{L}$ are:

$${}^{\mathcal{N}}\boldsymbol{F}_{\text{des}} = {}^{\mathcal{N}}\begin{bmatrix} F_1 \\ F_2 \\ 0 \end{bmatrix} \quad {}^{\mathcal{N}}\boldsymbol{L}_{\text{des}} = {}^{\mathcal{N}}\begin{bmatrix} 0 \\ 0 \\ L_3 \end{bmatrix} \tag{39}$$

From these equations an easy analytical solution for a valid joint configuration can be found using only ${}^{\mathcal{N}}\boldsymbol{F}$ through:

$$\boldsymbol{\theta} = g(\text{arctan2}(F_2, F_1)) \tag{40}$$

where g is a function that maps between the thrust direction and the arm angles. Once the joint angles are determined traditional thruster firing algorithms such as the Moore-Penrose pseudo-inverse[7,26,27] or linear programming[7,28] can be used to determine an optimal thruster firing that achieves the desired control wrench.

Torque Only Allocation The decoupled allocation approach detailed above relies on the requested force vector to determine the joint angles. This necessitates the determination of the optimal joint angle for scenarios where the desired control wrench is only non-zero for torques. The optimal set of joint angles will vary depending on the spacecraft configuration. Using the spacecraft detailed in Table 1 and Eq. (48) a Monte Carlo trial was run using the parameters in Table 2 to identify the joint angles that minimized the total required thruster force of the system.

Table 1: Spacecraft parameters

Parameter	**Symbol**	**Value**
Mass of the Hub	m_{hub}	330 kg
Body Frame Inertia of the Hub	${}^{\mathcal{B}}[I_{\text{hub},B_c}]$	$\begin{bmatrix} 82.1150 & 0 & 0 \\ 0 & 98.3950 & 0 \\ 0 & 0 & 121.0220 \end{bmatrix}$ kg·m^2
Body Frame Location of Hub Center of Mass	${}^{\mathcal{B}}\boldsymbol{r}_{B_c/B}$	$[0,0,0]^T$ m
Mass of Arm i	m_{a_i}	10 kg
Number of Thrusters per Arm	N_{thr}	2
Body Frame Location of Hinge 1	${}^{\mathcal{B}}\boldsymbol{r}_{H_1/B}$	$[0.79,0,0]^T$ m
Body Frame Location of Hinge 2	${}^{\mathcal{B}}\boldsymbol{r}_{H_2/B}$	$[-0.79,0,0]^T$ m
Arm Frame j Location of Arm j COM Relative to Hinge j	${}^{\mathcal{A}_\text{j}}\boldsymbol{r}_{A_j/H_j}$	$[0.75,0,0]^T$ m
Arm Frame j Location of Thruster i Relative to Hinge j	${}^{\mathcal{A}_\text{j}}\boldsymbol{r}_{T_i/H_j}$	$[1,0,0]^T$ m
Arm Frame j Thrust Unit Vector of Thruster 1	${}^{\mathcal{A}_\text{j}}\hat{g}_1$	$[0,1,0]^T$
Arm Frame j Thrust Unit Vector of Thruster 2	${}^{\mathcal{A}_\text{j}}\hat{g}_2$	$[0,-1,0]^T$
Arm Frame j Inertia of Arm j	${}^{\mathcal{A}_\text{j}}[I_{\text{a}_j,A_j}]$	$\begin{bmatrix} 0.0250 & 0 & 0 \\ 0 & 1.0542 & 0 \\ 0 & 0 & 1.0542 \end{bmatrix}$ kg·m^2
Body Frame to Hinge 1 Frame Direction Cosine Matrix (DCM)	$[BH_1]$	$\begin{bmatrix} 1 & 0 & 0 \\ 0 & 1 & 0 \\ 0 & 0 & 1 \end{bmatrix}$
Body Frame to Hinge 2 Frame DCM	$[BH_2]$	$\begin{bmatrix} -1 & 0 & 0 \\ 0 & -1 & 0 \\ 0 & 0 & 1 \end{bmatrix}$
Mean Total Spacecraft Inertia about the 3 axis	$I_{\text{sc,3,mean}}$	161.9083 kg·m^2
Minimum Joint Angle for Allocation of Joint j	θ_{min_j}	$-\frac{\pi}{2}$ rad
Maximum Joint Angle for Allocation of Joint j	θ_{max_j}	$\frac{\pi}{2}$ rad
Maximum Thrust from Thruster i	$f_{i,\text{min}}$	1.5 N
Maximum Motor Torque from Motor i	$u_{H_i,\text{max}}$	1.5 N·m

Figure 3 shows that for the spacecraft in Table 1 the inertia is at a maximum when the arms are both at 0° and is minimized when the arms are both at $\pm 90^\circ$. Despite this the total thruster force required to correct for a given error is minimized when the arms are at 0° as shown in Figure 4. Only cases where $\theta_1 = \theta_2$ were considered in Figure 4 since those are the only configurations capable of producing a pure torque solution for this spacecraft configuration. As such for this configuration the optimal joint angle for the torque only control wrench is $\theta_1 = \theta_2 = 0^\circ$.

Table 2: Torque only joint angle Monte Carlo parameters

Parameter	**Symbol**	**Value**
Hub Orientation Error	$\delta\phi$	$-5:5$ deg
Hub Angular Velocity Error	$\delta\dot{\phi}$	$-0.1:0.1$ rad/s
Desired Angular Acceleration	$\ddot{\phi}_{\text{des}}$	$-0.05:0.05$ rad/s^2
Environmental Torque	L_{env}	0 N·m
Number of Monte Carlo Trials	N_{trials}	100

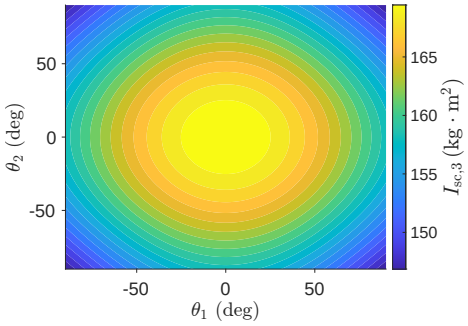

Figure 3: Total spacecraft inertia based on joint angles.

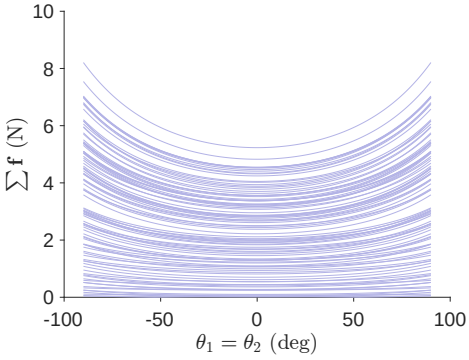

Figure 4: Total thruster force required for control torque.

Coupled and Decoupled Solution Comparison

To evaluate the quality of the decoupled solution a Monte Carlo trial was run comparing the results of the optimization shown in the coupled solution section to those found using the decoupled method detailed above. Table 1 details the parameters of the spacecraft used for this evaluation and Table 3 shows the parameters used for the Monte Carlo trial. To solve the optimization problem from the previous section the SQP option in MATLAB's *fmincon* was used with the default options except the optimality tolerance was lowered to 10^{-8} and the maximum function iterations was raised to 3000. A targeted multistart was used whenever *fmincon* failed to solve or if any component of the control wrench error $|\boldsymbol{u}_{\text{des}} - \boldsymbol{u}_{\text{control}}(\boldsymbol{\theta}, \boldsymbol{f})|$ exceeded 10^{-4}. To solve the decoupled approach Dual Simplex Highs in MATLAB's *linprog* was used with the default options.

Table 3: Joint and thruster allocation Monte Carlo parameters

Parameter	**Symbol**	**Value**
Control Weight Matrix	$\boldsymbol{W}_u$	$diag\{10^4\}$
Thrust Weight Matrix	$\boldsymbol{W}_f$	$10^{-2} \cdot \mathbf{1}$
Desired Force Magnitude	F_{mag}	$0.1:1.25$ N
Desired Force Direction	γ_{des}	$-\pi:\pi$ rad
Desired Torque	L_{des}	$-1:1$ N·m
Number of Monte Carlo Trials	N_{trials}	$9,960$

Figure 5 clearly shows the advantage of the decoupled solution. It is readily seen that the decoupled solution leads to a more accurate replication of the desired control while requiring approximately the same total thruster force and taking an order of magnitude less computation time.

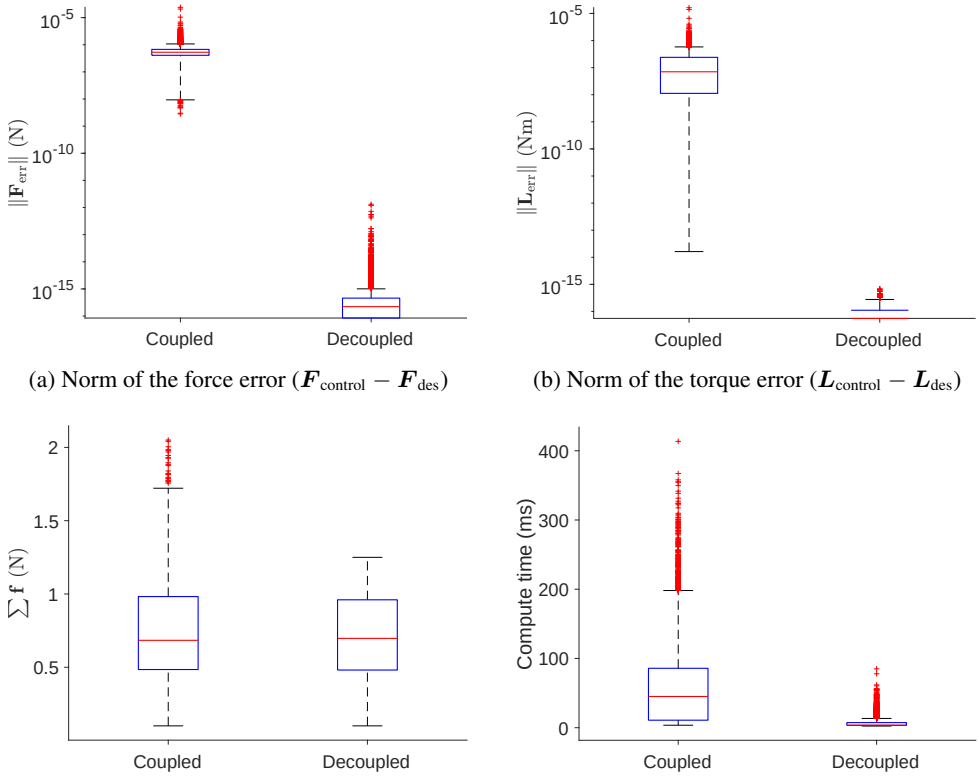

(a) Norm of the force error ($\boldsymbol{F}_{\text{control}} - \boldsymbol{F}_{\text{des}}$)

(b) Norm of the torque error ($\boldsymbol{L}_{\text{control}} - \boldsymbol{L}_{\text{des}}$)

(c) Total thrust

(d) Compute time

Figure 5: Comparison of performance metrics between coupled and decoupled allocation methods.

CLOSED LOOP CONTROL

This section focuses on the design of the control system for the 3-DOF planar control of the spacecraft. The cascaded control approach shown in Figure 6 is used where the outer control loop finds the desired control wrench which is fed into the joint angle and thruster firing allocation algorithm. This outputs the desired joint angles as well as firing times for each thruster. The desired joint angle is fed into the robotic arm controller which outputs the prescribed torque needed to negate hub accelerations. Once the joints reach their desired angle, the thrusters are fired based on the firing times output by the allocation algorithm. During this phase the joint motors provide the torque required to negate any arm accelerations. The process is then repeated until the system has reached its desired state.

Outer Control Loop

The outer loop controller is designed to track a reference trajectory $\dot{\boldsymbol{X}}_{\text{des}}$. Due to the decoupling of the translational motion in the problem from the rotational motion, the controller can be split into 2 parts.

Translational Control The translational controller is designed to drive $\delta\boldsymbol{x} = \boldsymbol{x} - \boldsymbol{x}_{\text{des}} \to 0$ and $\delta\dot{\boldsymbol{x}} = \dot{\boldsymbol{x}} - \dot{\boldsymbol{x}}_{\text{des}} \to 0$. Using $\boldsymbol{F}_{\text{ext}} = \boldsymbol{F}_{\text{env}} + \boldsymbol{F}_r$ where $\boldsymbol{F}_{\text{env}}$ are the forces from the environment and $\boldsymbol{F}_r$ is the thruster control forces Eq. (1) becomes:

$$\boldsymbol{F}_{\text{env}} + \boldsymbol{F}_r = m_{\text{sc}}\ddot{\boldsymbol{r}}_{C/N} \tag{41}$$

selecting the control to be:

$$\boldsymbol{F}_r = -[K]_{\text{trans}}\delta\boldsymbol{x} - [P]_{\text{trans}}\delta\dot{\boldsymbol{x}} + m_{\text{sc}}\ddot{\boldsymbol{x}}_{\text{des}} - \boldsymbol{F}_{\text{env}} \tag{42}$$

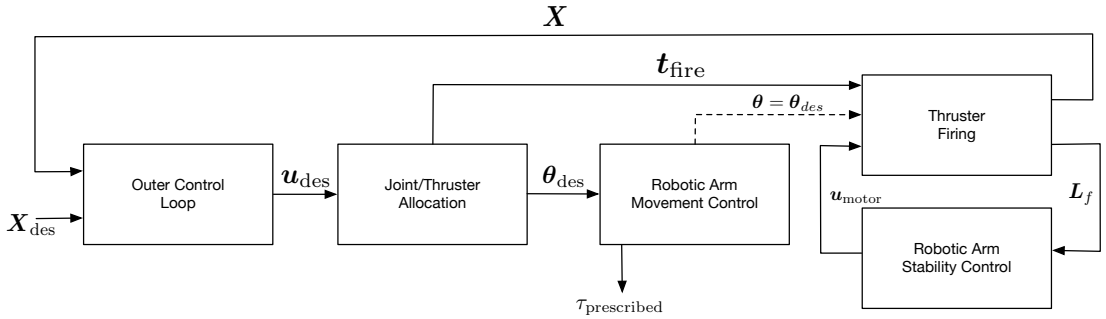

Figure 6: Control loop design

where $[K]_{\text{trans}}, [P]_{\text{trans}} \in \mathbb{R}^{2\times 2}$ are gain matrices for the translational motion. This leads to the closed loop dynamics:

$$\dot{\boldsymbol{e}} = [A]_{\text{trans}}\boldsymbol{e} \tag{43}$$

where:

$$\boldsymbol{e} = \begin{bmatrix} \delta\boldsymbol{x} \\ \delta\dot{\boldsymbol{x}} \end{bmatrix} \tag{44}$$

and:

$$[A]_{\text{trans}} = \begin{bmatrix} 0 & I_{2\times 2} \\ -\frac{1}{m_{\text{sc}}}[K]_{\text{trans}} & -\frac{1}{m_{\text{sc}}}[P]_{\text{trans}} \end{bmatrix} \tag{45}$$

This means the controller will be globally asymptotically stabilizing if $[K]_{\text{trans}}$ and $[P]_{\text{trans}}$ are positive definite matrices.

Hub Rotational Control The goal of hub rotational controller is to drive $\delta\phi = \phi - \phi_{\text{des}} \to 0$ and $\delta\dot{\phi} = \dot{\phi} - \dot{\phi}_{\text{des}} \to 0$. Assuming control gains are selected to enforce a separation in timescales, and leveraging the asymptotic stability of the arm controller as shown in the next section, the rotational EOM for the hub shown in Eq. (23) can be reduced to the standard planar rotational EOM for a rigid body:

$$I_{\text{sc},3}\ddot{\phi} = L_{\text{env}} + L_r \tag{46}$$

where L_{env} is the torque from the environment, L_r is the thruster control torque and:

$$L_{\text{env}} + L_r = \hat{n}_3 \cdot \boldsymbol{L}_B \tag{47}$$

selecting the control to be:

$$L_r = -K_{\text{rot}}\delta\phi - P_{\text{rot}}\delta\dot{\phi} + I_{\text{sc},3}\ddot{\phi}_{\text{des}} - L_{\text{env}} \tag{48}$$

where $K_{\text{rot}}, P_{\text{rot}} \in \mathbb{R}$ are the gains for the rotational motion and following the same steps as in the translational controller leads to:

$$[A]_{\text{rot}} = \begin{bmatrix} 0 & 1 \\ -\frac{1}{I_{\text{sc},3}}K_{\text{rot}} & -\frac{1}{I_{\text{sc},3}}P_{\text{rot}} \end{bmatrix} \tag{49}$$

As before this leads to the controller being globally asymptotically stabilizing if K_{rot} and P_{rot} are positive.

Robotic Arm Movement Control

The robotic arm movement control is designed to drive $\delta\boldsymbol{\theta} = \boldsymbol{\theta} - \boldsymbol{\theta}_{\text{des}} \to 0$ and $\dot{\boldsymbol{\theta}} \to 0$. During the movement it is assumed that the thrusters are inactive, so $\boldsymbol{F}_r = 0$ and $L_r = 0$. Additionally, a prescribed torque $\tau_{\text{prescribed}}$ is assumed to cancel any reaction torque due to arm acceleration, resulting in no hub accelerations. Under these assumptions the arm dynamics reduce to:

$$[M_\theta]\ddot{\boldsymbol{\theta}} = \boldsymbol{u}_H + \boldsymbol{C} \tag{50}$$

where $[M_\theta] \in \mathbb{R}^{(N_a \times N_a)}$ is the lower right hand corner of the full system mass matrix $[M] \in \mathbb{R}^{(N_a+1 \times N_a+1)}$, $\boldsymbol{u}_H \in \mathbb{R}^{N_a \times 1}$ is the vector of hinge motor control torques u_{H_i}, and $\boldsymbol{C} = [C_1, \cdots, C_{N_a}]^T$ with:

$$\begin{aligned} C_i =& \hat{n}_3 \cdot \boldsymbol{\tau}_{\text{ext}} + m_{\text{a}_i} d_i \dot{\phi}^2 \hat{a}_{i,2} \cdot \boldsymbol{r}_{H_i/B} \\ & - m_{\text{a}_i} d_i \hat{a}_{i,2} \cdot \left(\frac{\boldsymbol{F}_{\text{env}}}{m_{\text{sc}}} + \frac{\sum_{j=1}^{N_a} m_{\text{a}_j} d_j \dot{\theta}^2 \hat{a}_{j,1}}{m_{\text{sc}}} - 2\dot{\phi}\hat{n}_3 \times \boldsymbol{c}' - \dot{\phi}\hat{n}_3 \times (\dot{\phi}\hat{n}_3 \times \boldsymbol{c}) \right) \end{aligned} \tag{51}$$

Defining the Lyapunov function:

$$V(\delta\boldsymbol{\theta}, \dot{\boldsymbol{\theta}}) = \frac{1}{2}\dot{\boldsymbol{\theta}}^T \dot{\boldsymbol{\theta}} + \frac{1}{2}\delta\boldsymbol{\theta}^T [K_\theta] \delta\boldsymbol{\theta} \tag{52}$$

where $[K_\theta] \in \mathbb{R}^{(N_a \times N_a)}$ is a positive definite gain matrix. Taking the derivative leads to:

$$\dot{V}(\delta\boldsymbol{\theta}, \dot{\boldsymbol{\theta}}) = \dot{\boldsymbol{\theta}}^T (\ddot{\boldsymbol{\theta}} + [K_\theta]\delta\boldsymbol{\theta}) \tag{53}$$

due to $\dot{\boldsymbol{\theta}}_{\text{des}} = 0$. Forcing $\dot{V}$ to be negative semi-definite by setting it equal to $\dot{V}(\delta\boldsymbol{\theta}, \dot{\boldsymbol{\theta}}) = -\dot{\boldsymbol{\theta}}^T [P_\theta] \dot{\boldsymbol{\theta}}$ with $[P_\theta] \in \mathbb{R}^{(N_a \times N_a)}$ being another positive definite gain matrix and substituting in the value for $\ddot{\boldsymbol{\theta}}$ from Eq. (50) leads to:

$$\dot{\boldsymbol{\theta}}^T \left[[M_\theta]^{-1} (\boldsymbol{u}_H + \boldsymbol{C}) + [P_\theta]\dot{\boldsymbol{\theta}} + [K_\theta]\delta\boldsymbol{\theta} \right] = 0 \tag{54}$$

setting the term inside the brackets to zero and solving for the motor control torque vector produces the stabilizing control:

$$\boldsymbol{u}_H = [M_\theta](-[K_\theta]\delta\boldsymbol{\theta} - [P_\theta]\dot{\boldsymbol{\theta}}) - \boldsymbol{C} \tag{55}$$

The resulting control law renders the arm movement dynamics globally stable.

Asymptotic Stability To show the asymptotically stabilizing nature of the control, the method developed by Mukherjee and Chen[29] is utilized. The first derivative of the Lyapunov function is found to be zero on the set $\Omega : \{\dot{\boldsymbol{\theta}} = 0\}$. Taking the second derivative of V and evaluating over Ω leads to $\ddot{V} = 0$ since the value of $\ddot{\boldsymbol{\theta}}$ is bounded as previously proven. Finally taking the third derivative of V and evaluating over Ω leads to the negative definite expression:

$$\dddot{V} = -2((\boldsymbol{u}_H + \boldsymbol{C})^T [M_\theta]^{-1} [P_\theta] [M_\theta]^{-1} (\boldsymbol{u}_H + \boldsymbol{C})) \tag{56}$$

This shows that the control developed above is globally asymptotically stabilizing as required for the hub rotational control and with proper selection of $K_{\text{rot}}, P_{\text{rot}}, [K_\theta]$, and $[P_\theta]$ the separation of timescales can be ensured to allow the spacecraft to be treated as a rigid body in the outer control loop.

Prescribed Torque Calculation The robotic arm movement control above required a prescribed torque to be acting on the body to negate any potential hub accelerations. Using the $\boldsymbol{u}_H$ found by the controller it is possible to back solve for the $\tau_{\text{prescribed}}$ required to enforce this condition. Using the mass matrix to rewrite the three rotational EOMs and taking advantage of the thrusters being inactive leads to:

$$[M] \begin{bmatrix} \ddot{\phi} \\ \ddot{\boldsymbol{\theta}} \end{bmatrix} = \begin{bmatrix} \tau_{\text{prescribed}} \\ \boldsymbol{u}_H \end{bmatrix} + \begin{bmatrix} D \\ \boldsymbol{C} \end{bmatrix} \tag{57}$$

where:

$$\begin{aligned} D = L_{\text{env}} - \hat{n}_3 \cdot \Bigg(& \sum_{i=1}^{N_a} \left[2\dot{\phi} m_{\text{a}_i} d_i \theta_i \boldsymbol{r}_{A_i/B} \times (\hat{n}_3 \times \hat{a}_{i,2}) - m_{\text{a}_i} d_i \theta_i^2 \boldsymbol{r}_{A_i/B} \times \hat{a}_{i,1} \right] \\ & - m_{\text{sc}} \boldsymbol{c} \times \left(\frac{\boldsymbol{F}_{\text{env}}}{m_{\text{sc}}} + \frac{\sum_{i=1}^{N_a} m_{\text{a}_i} d_i \dot{\theta}_i^2 \hat{a}_{i,1}}{m_{\text{sc}}} - 2\dot{\phi}\hat{n}_3 \times \boldsymbol{c}' - \dot{\phi}\hat{n}_3 \times (\dot{\phi}\hat{n}_3 \times \boldsymbol{c}) \right) \Bigg) \end{aligned} \tag{58}$$

setting $\ddot{\phi} = 0$ and inverting $[M]$ so that:

$$[M]^{-1} = \begin{bmatrix} M^{\text{inv}}_{1,1} & \cdots & M^{\text{inv}}_{1,N_a+1} \\ \vdots & \ddots & \vdots \\ M^{\text{inv}}_{N_a+1,1} & \cdots & M^{\text{inv}}_{N_a+1,N_a+1} \end{bmatrix} \tag{59}$$

enables $\tau_{\text{prescribed}}$ to be found using:

$$\tau_{\text{prescribed}} = -D - \frac{1}{M^{\text{inv}}_{1,1}} \sum_{j=1}^{N_a} M^{\text{inv}}_{1,j+1}(u_{H_j} + C_j) \tag{60}$$

Application of this prescribed torque during arm movement enforces $\ddot{\phi} = 0$, thereby ensuring that the assumptions underlying the robotic arm movement controller remain valid.

Arm Control During Thruster Firing

Once the arms have reached their desired orientations and $\dot{\boldsymbol{\theta}} = \mathbf{0}$, the spacecraft transitions to the thruster firing phase to execute the outer-loop control objectives. During this phase, the hinge motors apply the torques necessary to counteract any torques induced at the joints by thruster activity. This maintains $\ddot{\boldsymbol{\theta}} = \mathbf{0}$, and together with the zero joint velocities, ensures that the spacecraft behaves as a rigid body throughout the thruster firing phase. Adjusting Eq. (57) to account for the thruster firing and removal of the prescribed torque leads to:

$$[M] \begin{bmatrix} \ddot{\phi} \\ \ddot{\boldsymbol{\theta}} \end{bmatrix} = \begin{bmatrix} L_r \\ \boldsymbol{u}_H + \boldsymbol{L}_f \end{bmatrix} + \begin{bmatrix} D \\ \boldsymbol{C} \end{bmatrix} - \begin{bmatrix} \hat{n}_3 \cdot (\boldsymbol{c} \times \boldsymbol{F}_r) \\ \boldsymbol{E} \end{bmatrix} \tag{61}$$

where $\boldsymbol{E} = [E_1, \cdots, E_{N_a}]^T$ and:

$$E_i = m_{\text{a}_i} d_i \hat{a}_{i,2} \cdot \frac{\boldsymbol{F}_r}{m_{\text{sc}}} \tag{62}$$

denoting the lower right $N_a \times N_a$ corner of $[M]^{-1}$ as $[M^{\text{inv}}_{\theta}]$ and building the vector $\boldsymbol{b} = [b_1, \cdots, b_{N_a}]^T$ where:

$$b_j = M^{\text{inv}}_{j,1}(L_r + D + \hat{n}_3 \cdot (\boldsymbol{c} \times \boldsymbol{F}_r)) + \sum_{k=1}^{N_a} M^{\text{inv}}_{j,k+1}(L_{f_k} + C_k + E_k) \tag{63}$$

the hinge motor torque vector can then be found using:

$$\boldsymbol{u}_H = -[M^{\text{inv}}_{\theta}]^{-1}(\boldsymbol{b}) \tag{64}$$

Applying these motor torques during thruster firing enforces $\ddot{\boldsymbol{\theta}} = \mathbf{0}$, ensuring that the spacecraft behaves as a rigid body throughout the firing phase, as assumed in the outer-loop control design.

NUMERICAL SIMULATION

This section presents numerical simulations of the 3-DOF planar spacecraft control system using thrusters mounted on robotic arms. Two scenarios are considered: regulation control and tracking control. The rectangular spacecraft for both simulations is detailed in Table 1 and is operating in a gravity free environment with no other external forces or torques. While the desired joint angles are selected within the range $\boldsymbol{\theta} \in [-\pi/2, \pi/2]$, the simulated joint dynamics are unconstrained and may exceed these bounds during arm motion. Table 4 shows the control gains used in both simulations. Both simulations use an outer loop control period of 10s with thruster actuation triggered once both $|\delta\boldsymbol{\theta}|, |\dot{\boldsymbol{\theta}}| < 10^{-4}$. A simple Discrete Pulse Thrusting using ROUND[30] firing algorithm was implemented with a minimum pulse time of 0.01s.

Table 4: Simulation control gains

Parameter	$[K_{\text{trans}}]$	$[P_{\text{trans}}]$	K_{rot}	P_{rot}	$[K_\theta]$	$[P_\theta]$
Value	$0.56I_{2\times2}$	$28I_{2\times2}$	0.4373	13.1193	$9.8696I_{2\times2}$	$9.4248I_{2\times2}$

Regulation Control

For the regulation control simulation the spacecraft was initialized to a position of $[1.2, -0.9]^T$ m, velocity of $[0.004, -0.005]^T$ m/s, hub attitude of 2 deg, and hub angular rate of 0.3 deg/s. All arm states were initialized to zero. The goal of the regulation control was to drive all non-arm states to zero while the final states related to the arms were left free.

Figure 7a shows the positional error of the spacecraft converging in around 200s while Figure 7b shows the attitude error converging in under 100s. Figures 8a and 8b show that translational and angular velocity errors converge within the first 100–200 seconds. Together Figures 7 and 8 confirm effective outer loop regulation control.

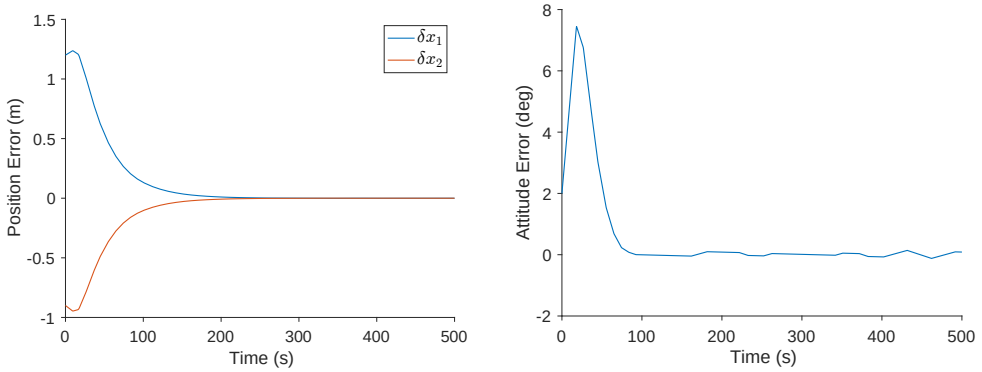

(a) Position error, $\delta \boldsymbol{x}$ (b) Attitude error, $\delta\phi$

Figure 7: Spacecraft center of mass position and hub attitude error

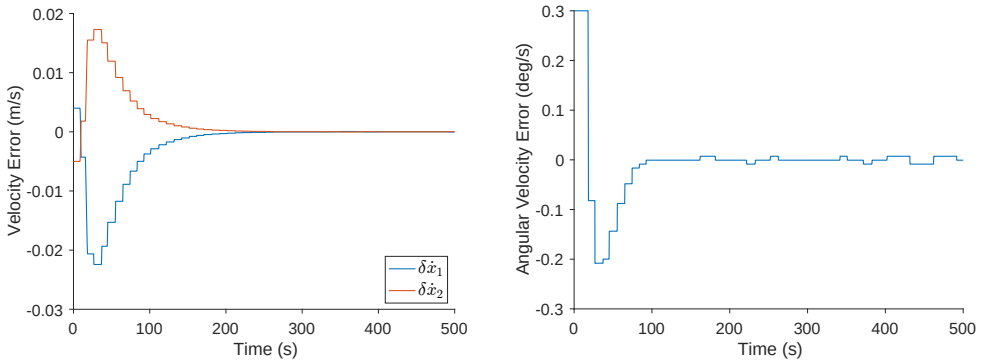

(a) Velocity error, $\delta \dot{\boldsymbol{x}}$ (b) Angular velocity error, $\delta\dot{\phi}$

Figure 8: Spacecraft center of mass velocity and hub angular velocity error

Figure 9a demonstrates the prescribed torque required to negate hub accelerations during arm movement. It can easily be seen that the required prescribed torques (peaking at upwards of 6 N·m) well exceed the

torques traditional momentum management devices like reaction wheels (RWs) can produce.[31] This implies that more complex devices such as variable speed control moment gyroscopes (VSCMGs) would be required to produce this torque. Figure 9b shows that the 3-DOF spacecraft control is achieved without exceeding the 1.5 Nm torque capability of the motors. Figure 10 demonstrates how both joint angles converge to the desired value in less than the 10 s control period leaving ample time for thruster firing during each control period.

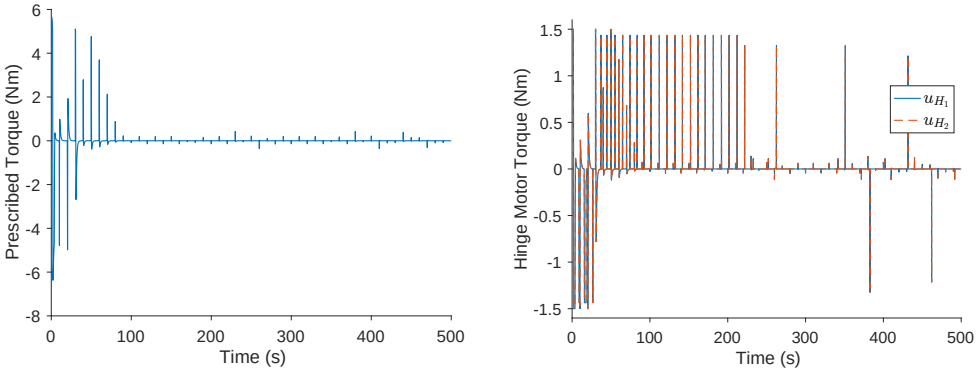

(a) Required prescribed torque, $\tau_{\text{prescribed}}$ (b) Hinge motor torques, $\boldsymbol{u}_H$

Figure 9: Prescribed torque and hinge motor torques

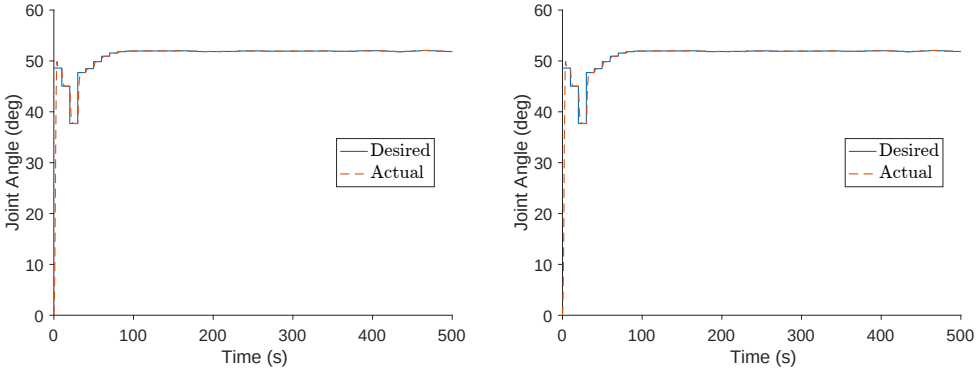

(a) Arm 1 joint angle, θ_1 (b) Arm 2 joint angle, θ_2

Figure 10: Joint angles over time. The solid line represents the desired joint angle, while the dashed line shows the actual angle achieved.

Tracking Control

For the tracking control simulation the spacecraft was initialized to a position of $[-10, -10]^T$ m, velocity of $[0.0064, -0.0093]^T$ m/s, hub attitude of 45 deg, and hub angular rate of -0.045 deg/s. All arm states were initialized to zero. The goal of the tracking problem was to mimic a 60 min close proximity inspection operation by flying the trajectory shown in Figure 11 while keeping the deputy spacecraft's northern face pointed at the chief spacecraft located at $(0, 0)$. The mean total spacecraft inertia about the 3 axis $I_{\text{sc},3,\text{mean}}$ was used as a constant value in Eq. (48).

Figure 12 demonstrates the very accurate position and attitude tracking of the outer loop control with the maximum positional error over the 60 min inspection being less than 25 mm and the max hub attitude error being less than 0.2 deg. Figure 13 shows similar tracking performance for the velocity and angular velocity.

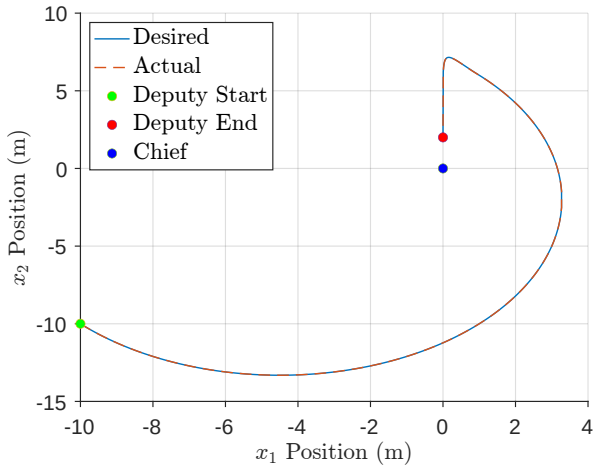

Figure 11: Spacecraft inspection trajectory. The solid line represents the desired trajectory, the dashed line represents the actual trajectory

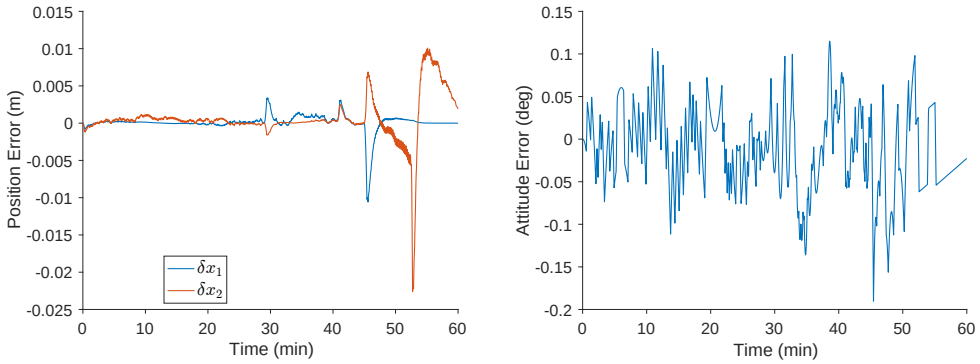

(a) Position error, $\delta \boldsymbol{x}$

(b) Attitude error, $\delta \phi$

Figure 12: Spacecraft center of mass position and hub attitude error

Figure 14a once again shows the prescribed torque exceeding the capabilities of most RWs. It also shows three large spikes of more than double the nominal prescribed torque, all of which correspond to the large joint angle changes (> 100 deg) seen in Figure 15. These large joint angle changes also lead to large overshoots in the actual joint angle when compared to the desired joint angle. Both the large prescribed torque and overshoot in joint angle could likely be addressed through input shaping within the robotic arm movement control in future work. Figure 14b once again shows that the maximum hinge motor torque is never exceeded. With the exception of the three instances of overshoot discussed above, Figure 15 shows that once again the joint angles accurately track their desired values.

The simulation results show the efficacy of the proposed robotic arm mounted thruster system with prescribed hub torque control system. The position, attitude, and rate errors all quickly converge to zero and stay there, allowing for accurate regulation and tracking control. The joint angles quickly converge to their desired values with minimal instances of large overshoot, enabling proper thruster alignment. The large prescribed torque values indicate a need to utilize more complex spacecraft hub attitude actuation capabilities such as VSCMGs for close proximity manuevers as opposed to the simpler and more traditional RWs that gave been shown to work for stationkeeping maneuvers.[12–16] The large prescribed torques also demonstrate the need for a subsystem to control hub motion during arm movement as the reaction torques that the subsystem would offset could lead to significant undesirable acceleration of the hub between thruster firings.

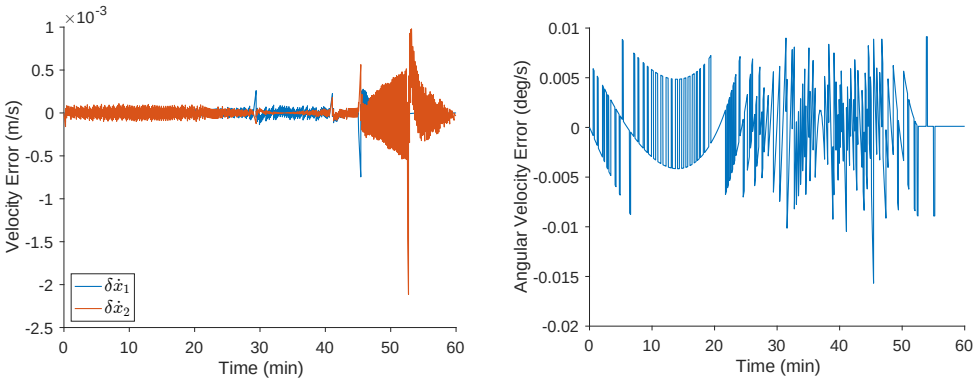

(a) Velocity error, $\delta\dot{\boldsymbol{x}}$ (b) Angular velocity error, $\delta\dot{\phi}$

Figure 13: Spacecraft center of mass velocity and hub angular velocity error

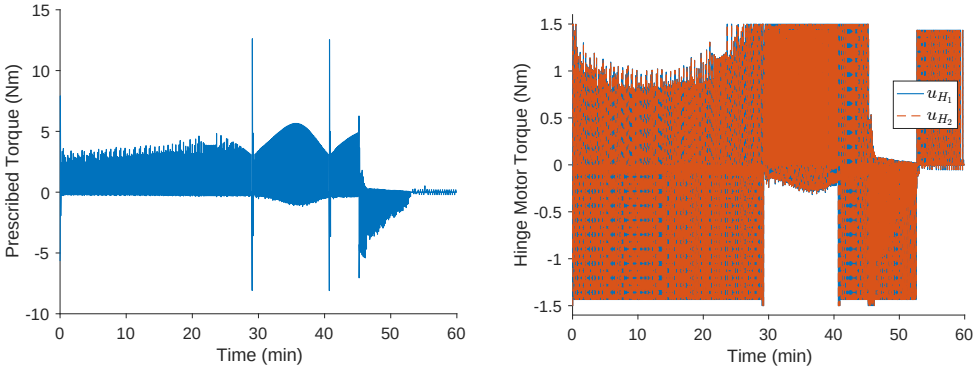

(a) Required prescribed torque, $\tau_{\text{prescribed}}$ (b) Hinge motor torques, $\boldsymbol{u}_H$

Figure 14: Prescribed torque and hinge motor torques

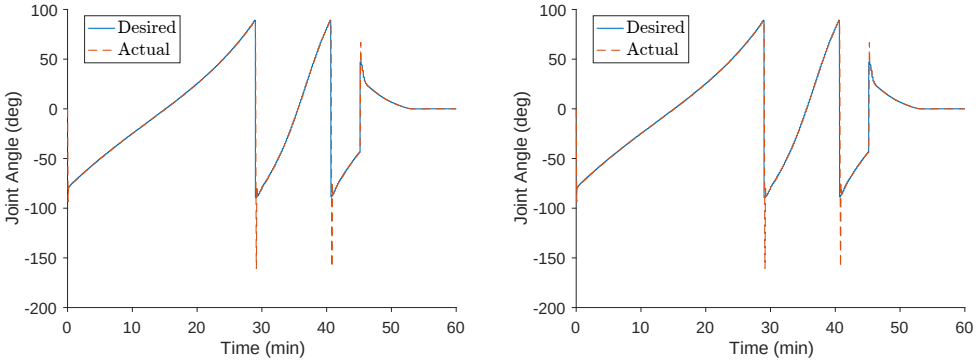

(a) Arm 1 joint angle, θ_1 (b) Arm 2 joint angle, θ_2

Figure 15: Joint angles over time. The solid line represents the desired joint angle, while the dashed line shows the actual angle achieved.

CONCLUSION

This paper presents a planar spacecraft control system employing thrusters mounted on robotic arms, incorporating prescribed torques to counteract hub accelerations induced by arm motion. The inclusion of these prescribed torques enables the use of reconfigurable thruster systems for close proximity operations. A cascaded control architecture was developed and its stability established using both linear analysis and Lyapunov methods. An expression for the prescribed torque required to negate hub acceleration was derived. Numerical simulations demonstrated high-accuracy position and attitude control in both regulation and trajectory tracking scenarios, validating the proposed method's effectiveness.

Future work will extend these methods to full 6-DOF spacecraft dynamics. Enhancements to the robotic arm controller, such as incorporating input shaping, will be explored to reduce large prescribed torques and mitigate joint overshoot. In addition, joint angle allocation strategies will be refined to minimize arm repositioning requirements and further improve control efficiency.

DISCLAIMER

The views expressed in this article are those of the author and do not reflect the official policy or position of the Department of the Air Force, Department of Defense, or the U.S. Government.

REFERENCES

[1] R. Mukherjee, "Survey Of Select Recent In-Space Servicing Assembly and Manufacturing Related Robotics Projects at The Jet Propulsion Laboratory," *ASCEND 2023*, Las Vegas, Nevada, American Institute of Aeronautics and Astronautics, Oct. 2023, 10.2514/6.2023-4700.

[2] D. D. Arney, J. Mulvaney, C. Williams, W. Ruperto-Hernández, J. Friz, C. Stockdale, J. Nelson, and R. Rivera-Vargas, "In-Space Servicing, Assembly, and Manufacturing (ISAM) State of Play," 2024.

[3] J. Lawless, S. Patane, R. Rollins, M. Ledbetter, and R. Cook, "Future ISAM Architectures for National Security Space," *ASCEND 2022*, Las Vegas, Nevada & Online, American Institute of Aeronautics and Astronautics, Oct. 2022, 10.2514/6.2022-4299.

[4] J. Rudico, J. T. Nichols, and G. Rogers, "Potential United States Space Force Mission Life Extension Applications," *AIAA SCITECH 2024 Forum*, Orlando, FL, American Institute of Aeronautics and Astronautics, Jan. 2024, 10.2514/6.2024-1067.

[5] J. L. Goodman, "History of Space Shuttle Rendezvous and Proximity Operations," *Journal of Spacecraft and Rockets*, Vol. 43, Sept. 2006, pp. 944–959, 10.2514/1.19653.

[6] M. Pasand, A. Hassani, and M. Ghorbani, "A Study of Spacecraft Reaction Thruster Configurations for Attitude Control System," *IEEE Aerospace and Electronic Systems Magazine*, Vol. 32, July 2017, pp. 22–39, 10.1109/MAES.2017.160104.

[7] F. Schmucker, "Development and Validation of an Efficient Thruster-Based Control Strategy for Orbital Robots," Master's thesis, Technical University of Munich, 2020.

[8] M. Fauré, D. Henry, J. Cieslak, P. Lachevre, and F. Ankersen, "Optimization of Spacecraft Thrusters Configuration Under Fault Diagnosability and Recoverability Constraints," *IEEE Transactions on Aerospace and Electronic Systems*, Vol. 59, Oct. 2023, pp. 5275–5286, 10.1109/TAES.2023.3256976.

[9] R. Staples, "Key Capabilities of Our Life Extension In-orbit (LEXI™) Servicer - Astroscale U.S.," Oct. 2021.

[10] A. Eisele, "Northrop Grumman's SpaceLogistics Continues Revolutionary Satellite Life-Extension Work with Sale of Third Mission Extension Pod," https://news.northropgrumman.com/news/releases/northrop-grummans-spacelogistics-continues-revolutionary-satellite-life-extension-work-with-sale-of-third-mission-extension-pod, 2023.

[11] R. Biesbroek, S. Aziz, A. Wolahan, S. Cipolla, M. Richard-noca, and L. Piguet, "The ClearSpace-1 mission: ESA and ClearSpace team up to remove debris," *8th European Conference on Space Debris*, 2021.

[12] R. J. Caverly, S. Di Cairano, and A. Weiss, "Split-Horizon MPC for Coupled Station Keeping, Attitude Control, and Momentum Management of GEO Satellites Using Electric Propulsion," *2018 Annual American Control Conference (ACC)*, June 2018, pp. 652–657, 10.23919/ACC.2018.8431329.

[13] R. J. Caverly, S. Di Cairano, and A. Weiss, "On-Off Quantization of an MPC Policy for Coupled Station Keeping, Attitude Control, and Momentum Management of GEO Satellites," *2018 European Control Conference (ECC)*, June 2018, pp. 1–6, 10.23919/ECC.2018.8550336.

[14] R. Caverly, S. Di Cairano, and A. Weiss, "Control Allocation and Quantization of a GEO Satellite with 4DOF Gimbaled Thruster Booms," *AIAA Scitech 2020 Forum*, Orlando, FL, American Institute of Aeronautics and Astronautics, Jan. 2020, 10.2514/6.2020-1687.

[15] D. Zlotnik, S. Di Cairano, and A. Weiss, "MPC for Coupled Station Keeping, Attitude Control, and Momentum Management of GEO Satellites Using on-off Electric Propulsion," *2017 IEEE Conference on Control Technology and Applications (CCTA)*, Aug. 2017, pp. 1835–1840, 10.1109/CCTA.2017.8062723.

[16] Z. Wei, T. Long, R. Shi, and X. Song, "Electric Thruster Configuration Design Optimization for Geostationary Satellites with Robotic Manipulators," *Advances in Space Research*, Vol. 69, May 2022, pp. 3798–3813, 10.1016/j.asr.2022.02.048.

[17] A. Prakash and D. K. Giri, "Design and Dynamical Analysis of a Novel 6-DOF Spacecraft Maneuvering System Using Robotic Manipulator-Based Thruster System," *AIAA SCITECH 2025 Forum*, Orlando, FL, American Institute of Aeronautics and Astronautics, Jan. 2025, 10.2514/6.2025-0408.

[18] D. Lee, J. E. Cochran, and T. S. No, "Robust Position and Attitude Control for Spacecraft Formation Flying," *Journal of Aerospace Engineering*, Vol. 25, July 2012, pp. 436–447, 10.1061/(ASCE)AS.1943-5525.0000146.

[19] M. Oda, "Coordinated Control of Spacecraft Attitude and Its Manipulator," *Proceedings of IEEE International Conference on Robotics and Automation*, Vol. 1, Apr. 1996, pp. 732–738 vol.1, 10.1109/ROBOT.1996.503861.

[20] L. Shi, J. Katupitiya, and N. Kinkaid, "A Robust Attitude Controller for a Spacecraft Equipped with a Robotic Manipulator," *2016 American Control Conference (ACC)*, July 2016, pp. 4966–4971, 10.1109/ACC.2016.7526140.

[21] I. M. Da Fonseca, L. C. S. Goes, N. Seito, M. K. da Silva Duarte, and É. J. de Oliveira, "Attitude Dynamics and Control of a Spacecraft like a Robotic Manipulator When Implementing On-Orbit Servicing," *Acta Astronautica*, Vol. 137, Aug. 2017, pp. 490–497, 10.1016/j.actaastro.2016.12.020.

[22] A. Antonello, A. Valverde, and P. Tsiotras, "Dynamics and Control of Spacecraft Manipulators with Thrusters and Momentum Exchange Devices," *Journal of Guidance, Control, and Dynamics*, Vol. 42, No. 1, 2019, pp. 15–29, 10.2514/1.G003601.

[23] R. Calaon, L. Kiner, C. Allard, and H. Schaub, "MOMENTUM MANAGEMENT OF A SPACECRAFT EQUIPPED WITH A DUAL-GIMBALLED ELECTRIC THRUSTER," *AAS Rocky Mountain GNC Conference*, 2023.

[24] H. Schaub and J. L. Junkins, *Analytical Mechanics of Space Systems*. Reston, VA: AIAA Education Series, 4th ed., 2018, 10.2514/4.105210.

[25] C. Allard, H. Schaub, and S. Piggott, "General Hinged Rigid-Body Dynamics Approximating First-Order Spacecraft Solar Panel Flexing," *Journal of Spacecraft and Rockets*, Vol. 55, Sept. 2018, pp. 1291–1299, 10.2514/1.A34125.

[26] H. Johansson, "Optimal Thruster Actuation in High Precision Attitude and Orbit Control Systems," Master's thesis, Technical University of Munich, 2005.

[27] S.-z. Yang, L. Wang, and P. Sun, "Optimal Thrust Allocation Logic Design of Dynamic Positioning with Pseudo-Inverse Method," *Journal of Shanghai Jiaotong University (Science)*, Vol. 16, Feb. 2011, pp. 118–123, 10.1007/s12204-011-1104-9.

[28] M. Tatiya, A. Banerjee, and R. Padhi, "Control Allocation for Reaction Thrusters of a Moon Lander Using Linear Programming ∗," *IFAC-PapersOnLine*, Vol. 51, Jan. 2018, pp. 633–637, 10.1016/j.ifacol.2018.05.106.

[29] R. Mukherjee and D. Chen, "Asymptotic Stability Theorem for Autonomous Systems," *Journal of Guidance, Control, and Dynamics*, Vol. 16, Sept. 1993, pp. 961–963, 10.2514/3.21108.

[30] J. Alcorn, H. Schaub, and S. Piggott, "Steady-State Attitude and Control Effort Sensitivity Analysis of Discretized Thruster Implementations," *Journal of Spacecraft and Rockets*, Vol. 54, Sept. 2017, pp. 1161–1169, 10.2514/1.A33709.

[31] V. Tan and V. St, "MATA-RL: Continuous Reaction Wheel Attitude Control Using the MATA Simulation Software and Reinforcement Learning," *35th Annual Small Satellite Conference*, 2021.